High-Resolution Observations of Microscale Influences on a Tornado Track Using Unpiloted Aerial Systems (UAS)

MELISSA A. WAGNER,[a,b] ROBERT K. DOE,[c] CHUYUAN WANG,[d] ERIK RASMUSSEN,[b,e] MICHAEL C. CONIGLIO,[e,f] KIMBERLY L. ELMORE,[b,e] ROBERT C. BALLING JR.,[a] AND RANDALL S. CERVENY[a]

[a] *School of Geographical Sciences and Urban Planning, Arizona State University, Tempe, Arizona*
[b] *Cooperative Institute for Mesoscale Meteorological Studies, University of Oklahoma, Norman, Oklahoma*
[c] *School of Environmental Sciences, University of Liverpool, Liverpool, United Kingdom*
[d] *Department of Geography and Environmental Planning, Towson University, Towson, Maryland*
[e] *NOAA/OAR/National Severe Storms Laboratory, Norman, Oklahoma*
[f] *School of Meteorology, University of Oklahoma, Norman, Oklahoma*

(Manuscript received 2 July 2020, in final form 21 May 2021)

ABSTRACT: Topography can have a significant influence on tornado intensity and direction by altering the near-surface inflow. However, past research involving topographic influence on tornadoes has shown significant variety in investigative approaches and conclusions. This study uses unpiloted aerial systems (UAS)–based high-resolution imagery, UAS-based 3D-modeling products, and correlation analyses to examine topographical influences on a portion of the 1 May 2018 Tescott, Kansas, EF3 tornado (EF indicates the enhanced Fujita scale). Two new metrics, visible difference vegetative index (VDVI) gap and VDVI aspect ratio, are introduced to quantify damage severity using UAS-based imagery and elevation information retrieved from a UAS-based digital surface model (DSM). Areas of enhanced scour are seen along the track in areas of local elevation maxima. Correlation analysis shows that damage severity, as measured by both VDVI gap and VDVI aspect ratio, is well correlated with increasing elevation. The VDVI gap is only weakly correlated with slope, and the VDVI aspect ratio is not correlated with slope. These findings are statistically significant at $p < 0.05$. As the tornado weakened in intensity, the path became nonlinear, traversing between two local elevation maxima. It is hypothesized that fast-moving intense flow formed and weakened as elevation increased over the short spatial distance. This research shows that topography and surface conditions are two of many important variables that should be considered when performing tornado-damage site investigations. It also illustrates the importance of UASs in detailed tornado analysis. VDVI gap and VDVI aspect ratio can provide insight into damage severity as a function of topography.

KEYWORDS: Tornadoes; Damage assessment; Geographic information systems (GIS); Local effects; Topographic effects; Statistical techniques

1. Introduction

Over recent years, the magnitude and severity of tornado impacts have generated costs into the billions of dollars and loss of lives. The challenges of accurate prediction and precise locational impact of tornadoes contribute to these costs by adding to the complexities of tornado forecasting and damage mitigation, especially with regard to vulnerability assessments. This is due, in part, to important concerns associated with varying tornado intensity, spatial scale, and surface conditions (e.g., land use or topography). Surface conditions can influence the direction and severity of a tornado track and are therefore an important consideration when assessing a local environment. The geotechnological application of unpiloted aerial systems (UASs) in enhanced site investigations can better address some of these challenges, especially in locations of complex terrain (Doe and Wagner 2019).

The history of research with regard to topographic influence on tornadoes is varied. Previous research has shown that topography can (i) initiate or enhance tornadogenesis (Passe-Smith 2006, 2008), (ii) affect tornado intensity (Coleman 2010; Bosart et al. 2006), (iii) alter path direction (Lewellen and Lewellen 2007; Tyrrell 2016), and (iv) influence the near-surface inflow to the tornado (Lewellen 2012; Karstens 2012). Forbes (1998) theorized that tornado intensity decreases on the windward (leeward) side of a ridge/hill due to the vortex compressing (stretching), creating mass convergence (divergence) and, consequently, a decrease (increase) in angular momentum (Lewellen 2012; Cannon et al. 2016). Lewellen (2012) expanded on this theory noting that the near-surface flow component would be deflected back into the vortex uphill, increasing near-surface flow and corner flow swirl ratio S_c and, consequently, decreasing tornado intensity. In addition to changes in damage severity, Lewellen (2012) also noted a tornado path could deviate to the left or right as it respectively ascends or descends the ridge. While Lewellen (2012) and Coleman (2010) observed similar results as Forbes (1998), Lewellen (2012) also found a brief intensification in simulated tornado intensity near the ridge citing surface roughness, translational velocity, storm velocity, and slope as important factors in altering near surface flow and S_c.

Other studies using radar analyses, aerial-photography and satellite-based damage assessments, and numerical modeling have shown mixed results in topographic influences on tornadoes. Although Houser et al. (2020) found a statistically significant

Corresponding author: Melissa A. Wagner, mawagner@ou.edu

DOI: 10.1175/MWR-D-20-0213.1

relationship between elevation change and tornado intensity in their radar-based analysis, this relationship varied and was therefore suggested to be case-specific. Cannon et al. (2016) found greater damage severity on the windward side versus the leeward side using high-resolution aerial photography but noted large variability in damage between the windward and leeward sides. They also noted that the relationship between damage severity and elevation change was more pronounced in areas of shallower slopes, suggesting other factors were at play. Ahmed (2016) noted a zone of protection on the leeward side approximately 5 times the height of the hill (elevation gain), suggesting tornado diameter had to be larger than the depression for leeward protection, using a combination of satellite-based and ground-based damage assessments with numerical modeling. Satrio et al. (2020) also used numerical modeling and found that the topography can influence path direction, vortex contraction/expansion, and vortex tilt, similar to the findings of Lewellen (2012). Numerical simulations, however, are limited by model configuration and representation of topography, whereas satellite-based damage assessments can be too coarse to resolve local extreme wind impacts.

High-resolution damage assessments utilizing UAS technologies can provide better analysis of topographic influences on tornadoes at the microscale. UAS technologies provide centimeter-scale information because of their low altitude collection of less than 400 ft (122 m) above ground level (AGL) (Womble et al. 2018; Wagner et al. 2019). This detailed information coupled with the three-dimensional (3D) modeling capabilities of UAS via structure from motion (SfM) can lead to a better insight into high-wind interactions with land cover and topography (Wagner et al. 2019). SfM is a technique that utilizes overlapping two-dimensional (2D) imagery to reconstruct 3D scenes and produce 2D modeling products (e.g., orthomosaics) and 3D modeling products [e.g., digital surface models (DSMs) and point clouds], which contain geographic coordinates and elevation information (Westoby et al. 2012; Carrivick et al. 2016). This approach is a cost-effective alternative to lidar (Westoby et al. 2012; Johnson et al. 2014) and has been used in estimating fault line movement (Heredia et al. 2009; Johnson et al. 2014) as well as assessing typhoon (Ezequiel et al. 2014; Chen et al. 2020) and tornado damage (Wagner and Doe 2017; Womble et al. 2018).

In addition to 3D modeling, UAS image enhancements can better depict the extent and variability of damage. Typically, normalized difference vegetation index (NDVI) is used to assess vegetation health due to the high contrast in spectral reflectance between the near-infrared band and the red band (Carlson and Ripley 1997). Spectral reflectance of healthy vegetation in the near-infrared band is nearly 10 times that of the red band because of the spongy mesophyll (Kingfield and de Beurs 2017). However, when near-infrared information is unavailable, visible difference vegetation index (VDVI), which uses information in the visible bands (blue, green, and red), can be used in place of NDVI by substituting information obtained in the green band for the near-infrared band (Wang et al. 2015). VDVI has a relatively high accuracy in comparison with NDVI (Xue and Su 2017) and has been used to monitor vegetation health (Du and Noguchi 2017) and soil erosion (Huang 2018). VDVI imagery in conjunction with elevation information obtained from UAS technologies could better depict land cover changes associated with high wind events.

Performing high-resolution site investigations can lead to a better understanding of how specific surface conditions such as topography can influence tornado dynamics and damage path characteristics. This study uses UAS-based high-resolution imagery and UAS-based 3D-modeling products to examine topographical influences on a portion (pathlength of approximately 550 m) of the 1 May 2018 EF3 Tescott, Kansas, tornado, where the greatest elevation change (approximately 54 m or 177.2 ft) occurred (EF*X* indicates the rating on the enhanced Fujita scale). Two metrics, VDVI gap and VDVI aspect ratio, were introduced to quantify damage severity based on UAS VDVI imagery and elevation information retrieved from the UAS-based DSM. Spatial comparisons, overlay analysis (see McHarg 1969), and transect analysis of UAS-based visible imagery, VDVI imagery, and DSM information were performed to assess topographical influences and terrain effects on a portion of the tornado track. In addition, correlations were used to examine the strength of the relationship between damage severity, as measured by VDVI gap and VDVI aspect ratio, and elevation, slope, and path width. These analyses give new information on the microscale influence of topography on tornadoes and present one of the first detailed UAS-based tornado/topographic studies to appear in refereed literature.

2. Methods

a. Study area

On 1 May 2018, five supercells affected north-central Kansas, spawning 12 tornadoes. One supercell near Tescott produced an EF3-rated tornado with a damage pathlength of 23.3 km (14.5 mi) and maximum width of 0.8 km (0.5 mi) (see Fig. 1) (NOAA/National Centers for Environmental Information 2020). Although no injuries or deaths were reported, this tornado produced isolated severe damage to property and vegetation within this sparsely populated region. The analysis presented here focuses on the portion of the path (pathlength of approximately 550 m) with the greatest elevation change (approximately 54 m or 177.2 ft).

b. Data collection

Following the tornado, UAS surveys were conducted to obtain poststorm visible imagery. A DJI Phantom 4 Pro UAS equipped with a 20-megapixel visible camera was flown at a flying height of 76.2 m (250 ft), yielding imagery with 1.69-cm spatial resolution per pixel. Visible imagery was collected using the flight-planning software DroneDeploy with a near nadir angle and 75% front and side overlap to achieve 3D modeling capabilities through SfM (e.g., Westoby et al. 2012; Johnson et al. 2014). Approximately 2000 images were collected from 18 to 20 May 2018 under relatively cloud free skies and during optimal illumination conditions (low zenith angle) that minimized cloud shadows (see Tmušić et al. 2020).

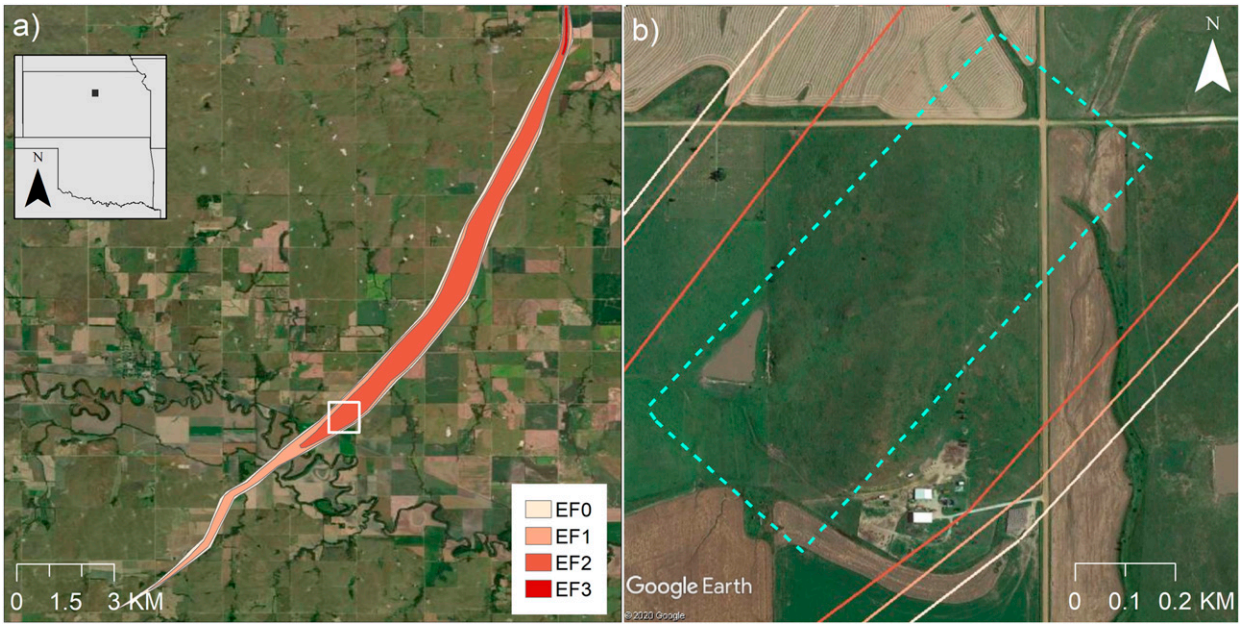

FIG. 1. The 1 May 2018 Tescott tornado path (a) overview and (b) survey site, outlined with the dashed cyan line. The white-outlined box in (a) corresponds to the photograph area of (b). Isolines show damage ratings according to the enhanced Fujita (EF) scale, with the heaviest damage (EF3) shown in red and the weakest damage (EF0) shown in beige.

Ground control surveys were conducted to ensure geospatial accuracy of data. Ground control points (GCPs) were collected using Trimble Geo7x ground control survey equipment with global navigation satellite system and global positioning system (GPS) capabilities. This system enabled high-accuracy ground surveying and precise point measuring with an accuracy of ±0.4 cm. The 10 points (GCPs) were collected using 1 m × 1 m targets, which were distributed throughout the study area and at varying elevation heights. Horizontal positions were referenced to 1984 World Geodetic Datum universal transverse Mercator (UTM), and vertical positions were referenced to World Geodetic System 1984 (WGS 84). GCPs were converted to UTM zone 14 north (UTM 14N) to align with the UAS data.

c. *Data preprocessing*

UAS imagery was processed using Agisoft Metashape Professional (Agisoft 2019) to generate postevent imagery and 3D-modeling products (DSM and point cloud). UAS images were coregistered to GCPs to remove positional distortions of 1–10 cm, resulting from errors in camera GPS location (Johnson et al. 2014). Color corrections were performed using the calibrate color algorithm in Agisoft Metashape Professional to balance brightness values over the entire dataset due to differences in illumination conditions. UAS-derived products included dense point clouds, DSM, and an orthomosaic, which is a geometrically corrected aerial image that provides an accurate representation of an area and can be used to measure true distances.

VDVI was employed to better identify high wind damage. VDVI can be used to assess vegetation health and identify land cover types (e.g., bare soil and vegetation) based on the spectral response of features and information obtained in the visible bands (blue, green, and red) (Wang et al. 2015). VDVI values range between −1 and 1, similar to NDVI, where index values close to 1 are indicative of healthy vegetation; index values close to 0 are indicative of bare soil; and negative index values are indicative of water. VDVI was calculated using

$$\mathrm{VDVI} = \frac{2 \times \mathrm{Green} - \mathrm{Red} - \mathrm{Blue}}{2 \times \mathrm{Green} + \mathrm{Red} + \mathrm{Blue}}, \tag{1}$$

where Green, Red, and Blue represent pixel digital numbers, which range from 0 to 255, for the green band, red band, and blue band imagery collected by the sensor.

d. *Assessments of microscale influences on tornadoes*

First, spatial comparisons, overlay analysis, and transect analyses were used to examine topographic influences on tornadoes. The UAS-based orthomosaic was compared with elevation information obtained from the UAS-based DSM to examine high wind interactions with microtopographic features. In a geographic information system (GIS) platform, 1- and 2-m elevation contours were generated using the UAS-based DSM and overlaid onto the VDVI image to assess the location and extent of scour relative to elevation changes. Slope, here defined as the absolute maximum rate of elevation change, was calculated to quantify changes in elevation gradient. Slope was computed as the absolute value of percent rise using the UAS-based DSM and a 3 × 3 window (pixel neighborhood) around the center pixel, where absolute maximum change in elevation is calculated

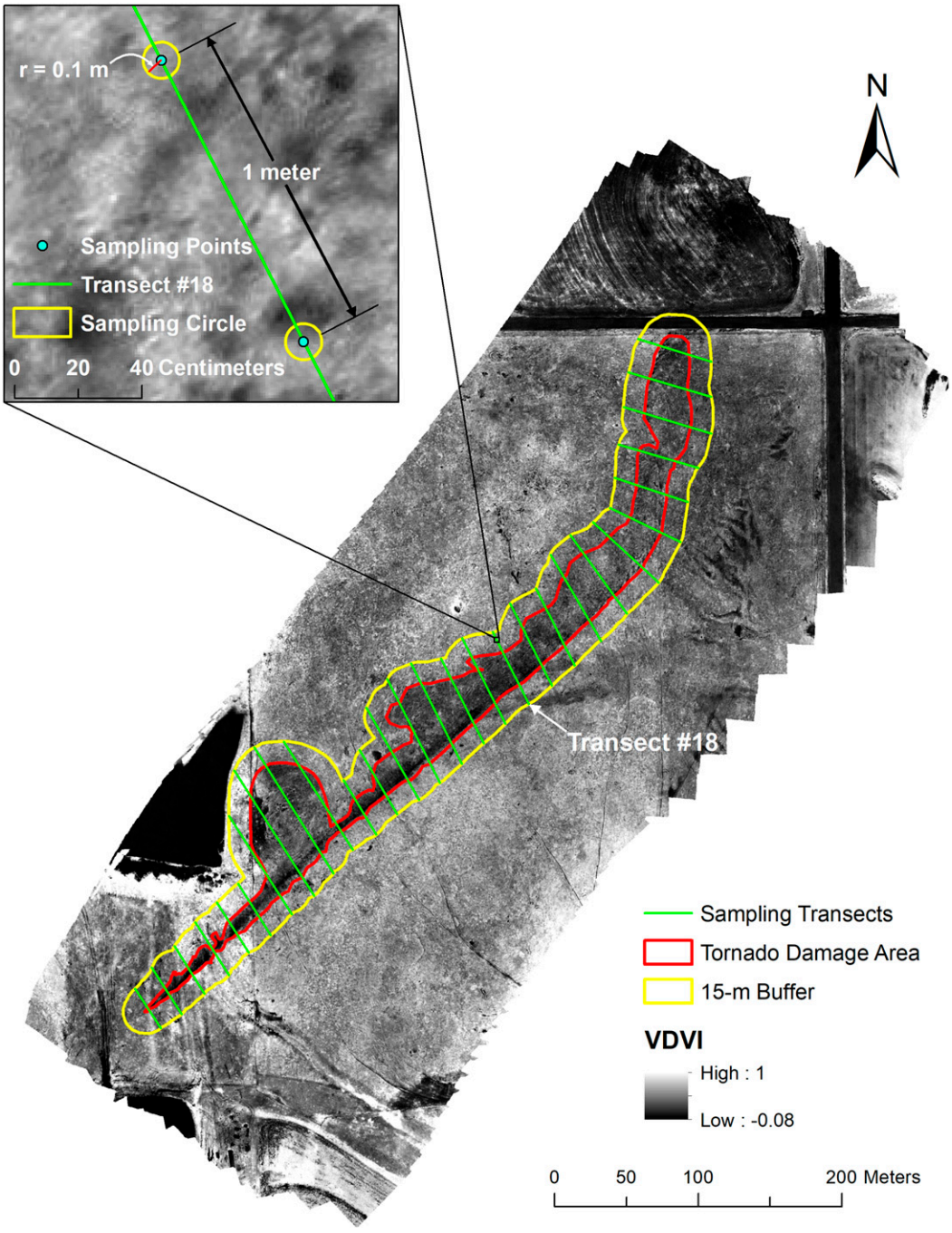

FIG. 2. VDVI image of the 1 May 2018 Tescott tornado survey site (see Fig. 1b). Transects are shown in green oriented nearly perpendicular to the tornado track, the boundary of the tornado-damaged area is outlined in red, and a 15-m buffer around the boundary is outlined in yellow. The inset in the top-left corner shows sampling points and circles, displayed in blue and yellow, respectively, that were used to extract VDVI, elevation, and slope values along transect 18.

between the pixel and its neighbors. It is important to note that the calculation of slope in a GIS platform does not consider the directionality of movement (i.e., uphill or downhill), but only the absolute value of slope in degrees or a percentage. In addition to slope, hillshade, which enhances 3D appearance of terrain by using patterns of light and shadows, was generated to assess terrain effects and surface scour.

Variability of damage relative to elevation was evaluated using 1) transects oriented nearly perpendicular to the

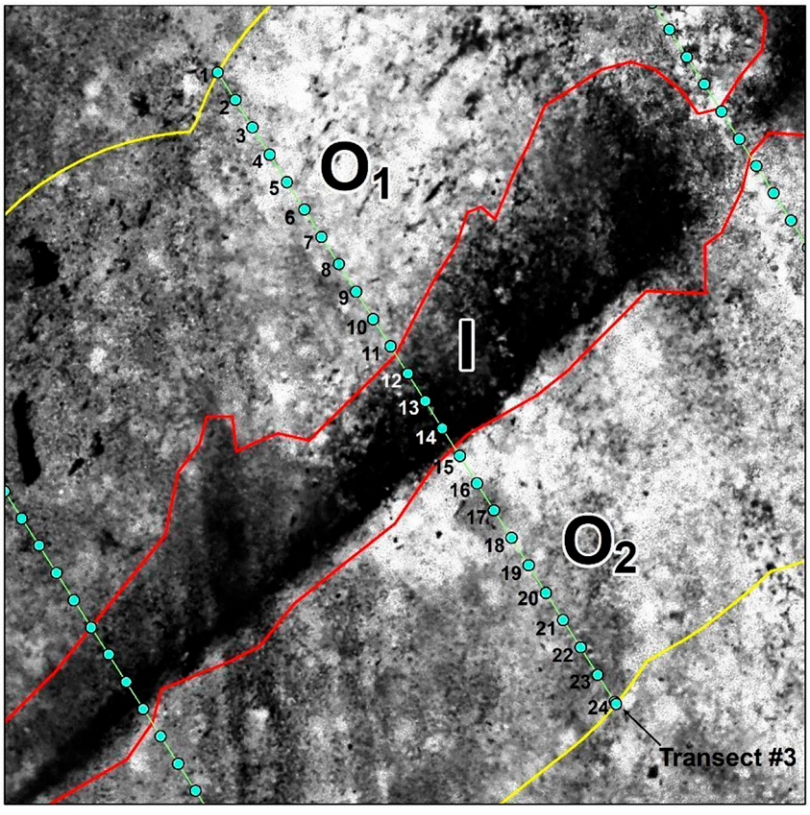

(a)

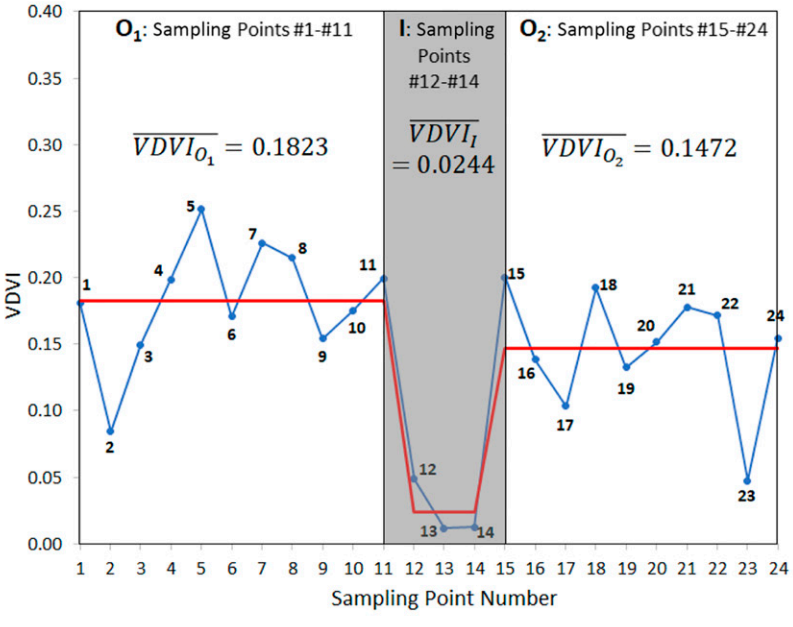

$$VDVI\ Gap = \frac{0.1823 + 0.1472}{2} - 0.0244 = 0.1404$$

(b)

FIG. 3. Illustration of calculations for VDVI gap, a metric for estimating damage severity along each transect (see Fig. 2). (a) Sampling points along transect 3 within the buffer (O_1 and O_2) and damaged area (I) (see Fig. 2). (b) VDVI values obtained from each sampling point in (a) (blue line). Mean VDVI values for O_1, O_2, and I are shown as red line segments.

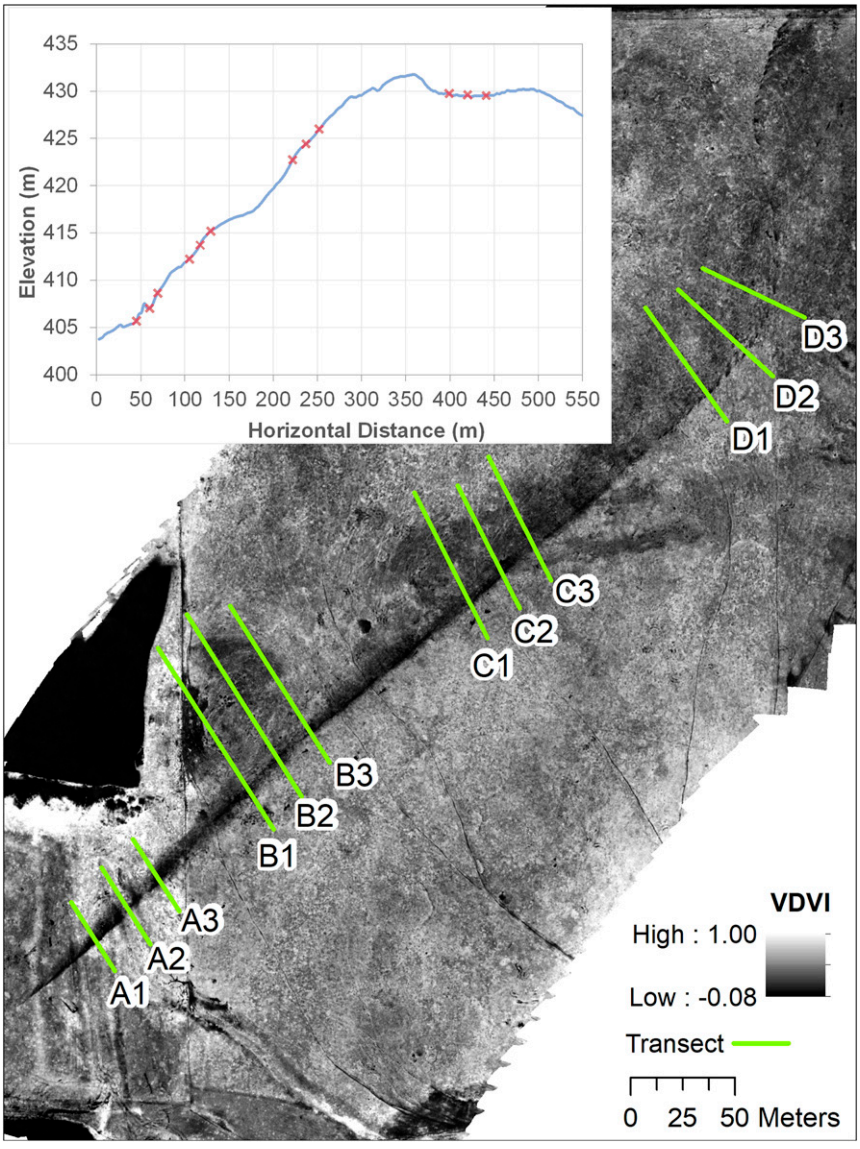

FIG. 4. VDVI image of the 1 May 2018 Tescott tornado survey site with transects, shown in green, oriented nearly perpendicular to the tornado track. The inset in the top-left corner shows the vertical elevation profile along the center of the damage path (the area of greatest scour). Red crosses correspond to the location of the selected transects at key elevation profiles discussed in the main text and labeled in the VDVI image.

centerline of the damage path and 2) simple correlation analysis (see Fig. 2). First, the boundary of the tornado-damaged area (red line in Fig. 2) was delineated. A 15-m buffer (yellow line in Fig. 2) was created around the boundary based on an average path width of 30 m. This buffer, which has a total width of 30 m, serves as a control to effectively compare vegetation directly affected by tornadic winds inside the tornado-damaged area relative to vegetation outside the tornado-damaged area. Transect lines were drawn nearly perpendicular to the tornado path across the buffer region to include damaged and nondamaged areas of the tornado path (see Fig. 2). These transects were placed at 20-m intervals, for a total of 30 transects.

VDVI, elevation, and slope values were extracted using sampling circles along these transects. Sampling points (blue dots shown in the inset in Fig. 2) were placed at 1-m intervals along each transect to obtain approximately 60 sample points per transect for statistical analysis. Sampling pixels from VDVI, DSM, and slope imagery were extracted using a sampling buffer of 0.1-m radius around each sampling point (yellow circles in the smaller image in Fig. 2), yielding approximately 160 pixels within each sampling circle. Mean VDVI, elevation,

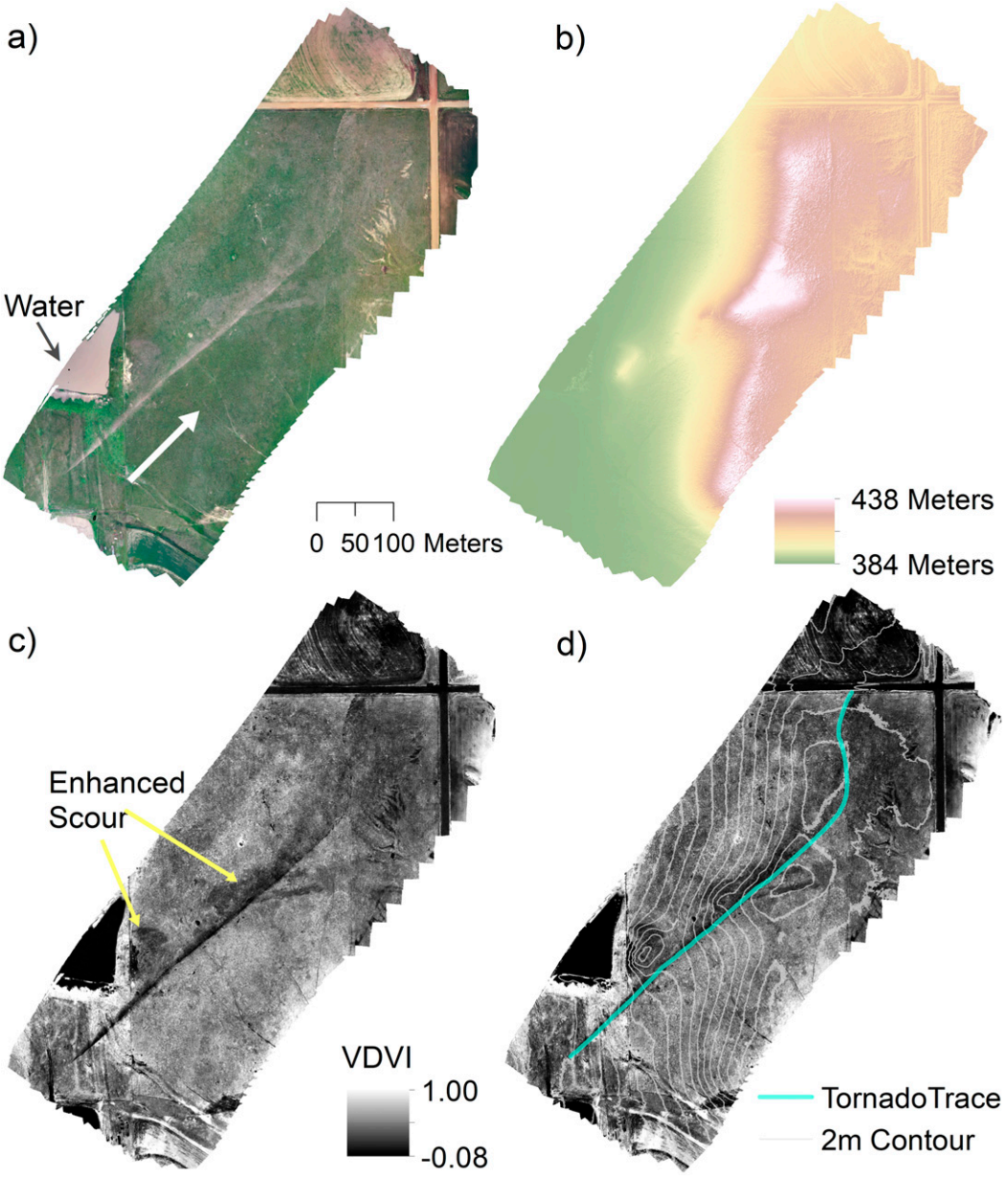

FIG. 5. UAS-based information of the 1 May 2018 Tescott tornado survey site (see Fig. 1): (a) true-color composite image, (b) digital surface model (DSM), (c) VDVI image, and (d) VDVI image overlaid with 2-m contours (gray lines) and the tornado trace (centerline of damage path shown as blue line). In (a), the white arrow shows the direction that the tornado traveled from southwest to northeast, and the black arrow points to water. Yellow arrows in (c) point to areas of enhanced scour in areas of local elevation maxima.

and slope values were calculated for each sampling circle to minimize noise in the imagery external to tornado damage. For each transect, path width (width within the tornado-damaged area; see Fig. 2), mean elevation, and mean slope were computed.

Two new metrics, VDVI gap and VDVI aspect ratio, are introduced to quantify damage severity for each transect. VDVI gap provides a one-dimensional metric of damage severity (magnitude: scalar), whereas VDVI aspect ratio includes an estimation of the area affected (dimensions). Figure 3 illustrates the calculation of VDVI gap using transect 3 as an example and the following equation:

$$\text{VDVI Gap} = \frac{\overline{\text{VDVI}_{O_1}} + \overline{\text{VDVI}_{O_2}}}{2} - \overline{\text{VDVI}_{I}}. \qquad (2)$$

Mean VDVI values are calculated within the damage area (I) and inside the 15-m buffer (O_1 and O_2) (see the red line segments in Fig. 3). VDVI gap is the difference between the

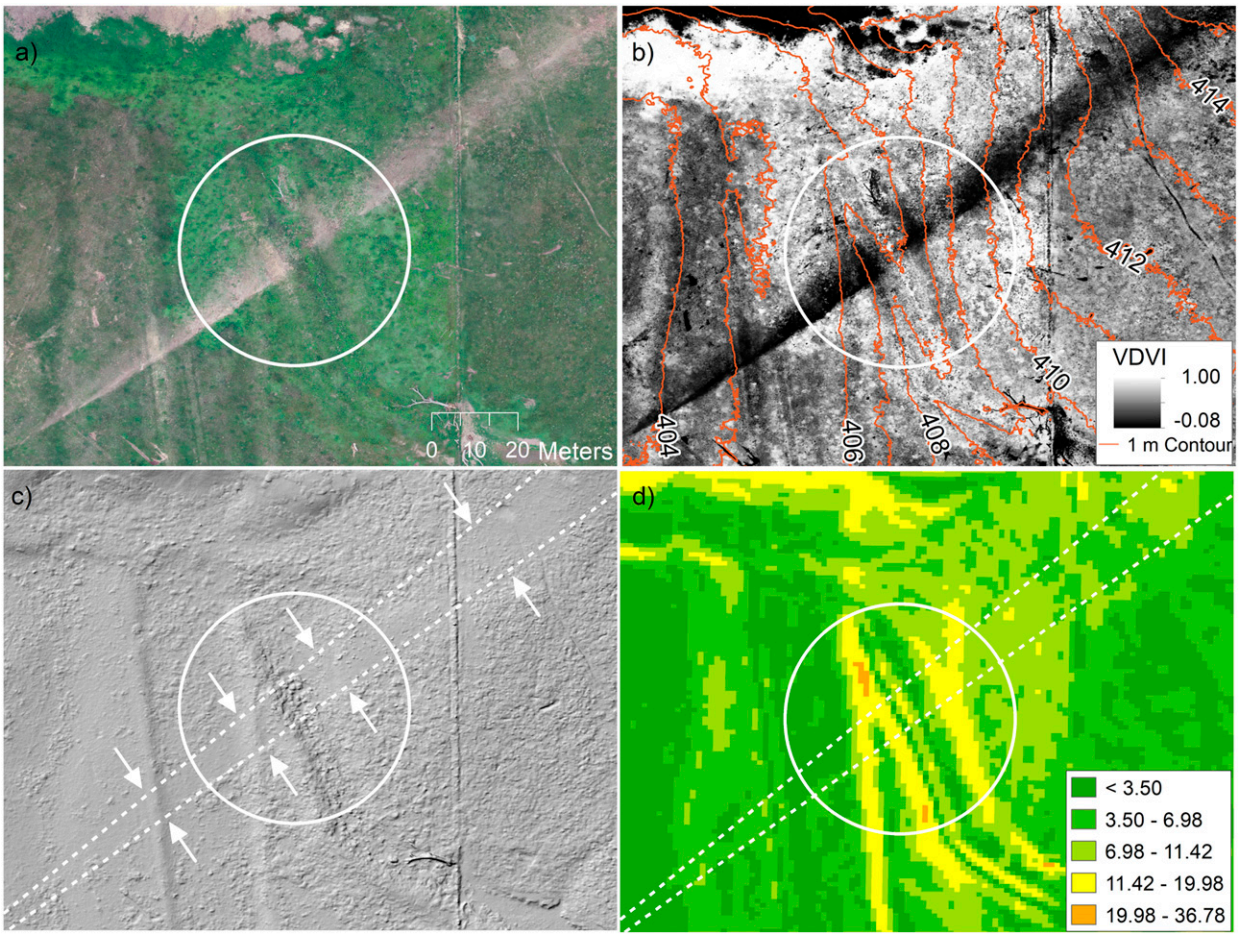

FIG. 6. Microtopographical influences of high-wind impacts captured in (a) true-color composite image, (b) VDVI image overlaid with 1-m contours (orange lines), (c) hillshade, and (d) slope of the 1 May 2018 Tescott tornado survey site. The visible break in the damage path (highlighted in the white-outlined circle) is due to limited surface erosion [increased texture in (c)] with the sunken gully. White arrows pointing to smoothed surfaces within white dashed lines (the tornado track) in (c) show areas of the enhanced scour within shortgrass prairie.

mean VDVI value within the damage area ($\overline{\text{VDVI}_\text{I}}$) and the average of the two mean VDVI values inside the 15-m buffer ($\overline{\text{VDVI}_{\text{O}_1}}$ and $\overline{\text{VDVI}_{\text{O}_2}}$) (see Fig. 3). VDVI gap assesses damage severity (or degree of change) along the damage path by comparing the mean VDVI values inside the area of enhanced scour with the background values, where damage is minimal or absent.

VDVI aspect ratio considers damage severity and the area affected (path width). This metric is similar to aspect ratio in geometry, which considers one dimension divided by another dimension. Here, VDVI aspect ratio is calculated by dividing VDVI gap by path width using the following equation:

$$\text{VDVI aspect ratio} = \frac{\text{VDVI Gap}}{\text{path width}}. \tag{3}$$

VDVI gap, while a measure of damage severity, also can be viewed as a dimension of depth. Higher VDVI aspect ratios would correspond to large damage gradients concentrated over smaller area, whereas lower VDVI aspect ratios values correspond to smaller damage gradients concentrated over larger area. This metric may better assess the relationship of damage severity, path width, and elevation.

The relationship of damage severity and path width with elevation and slope was evaluated using nonparametric bootstrapping (Efron and Tibshirani 1994) simple correlation. We generated 5000 bootstrap replicates and applied bootstrap tiling (also known as importance sampling; Efron 1981; DiCiccio and Romano 1990; Hesterberg 1999) to ensure the proper confidence interval coverages. If the confidence interval contains zero, the correlation is considered to be statistically zero and no further statistical treatment is warranted.

In addition to correlation analysis, changes in damage severity were assessed, as measured by VDVI values, and path width at key elevation profiles (Fig. 4). Transects were selected at the gully (group A), near areas of local slope change (groups B and C), and at the top of the hill (group D) to assess changes

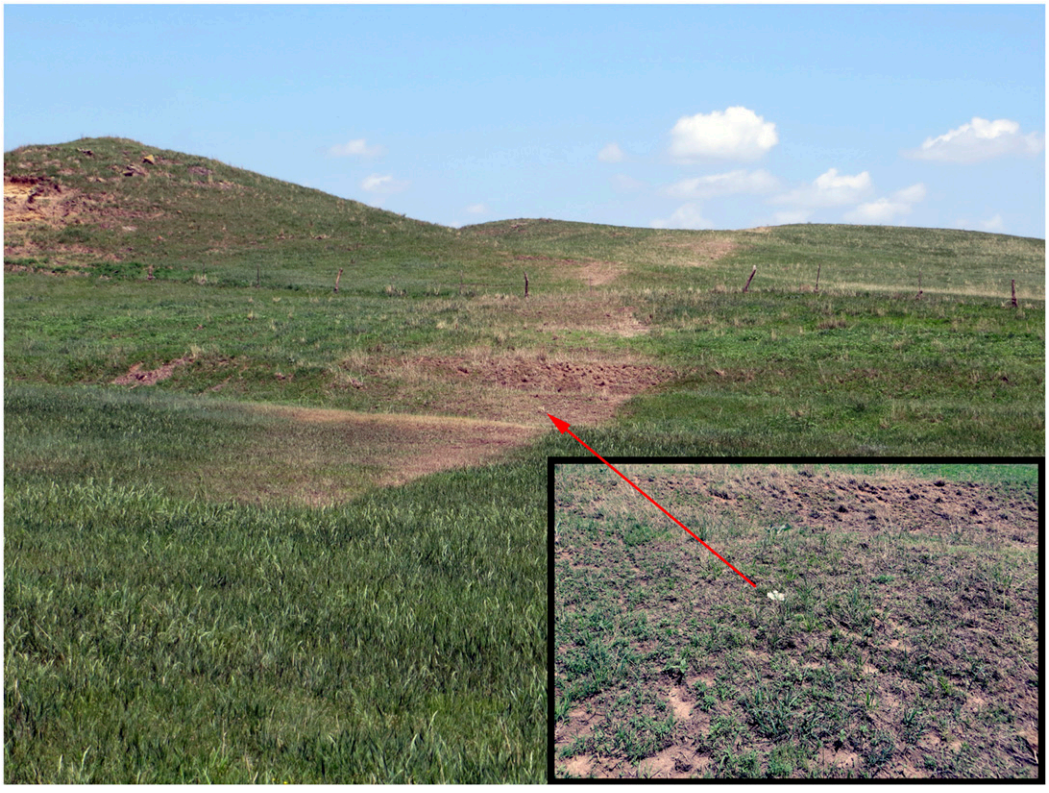

FIG. 7. The tornado track is visible to the human eye as it progresses uphill. The inset image from the ground survey (bottom-right corner) shows distinct scour to uniform vegetation and dry conditions inside the gully. The image is taken from the center of the track within the gully. The red arrow points to a corresponding white marker for reference.

in damage relative to local elevation minimum (group A) and maximum (group B), steep elevation gradient (group C), and flat terrain (group D), respectively (see Figs. 4, 5b). For each group, three transects were selected to capture the sensitivity of damage severity to elevation changes, including microscale changes as seen with the dip in elevation in group A. Mean VDVI and elevation values were plotted for each selected transect and group to assess changes in damage variability as a function of elevation.

4. Results

a. Spatial assessments of microscale influences on tornadoes

Both visible and VDVI images (Figs. 5a,c) show an area of enhanced scour starting at the initial point (bottom of the image), continuing through the center of the image, and then decreasing in intensity as the track visibly fans out. In the imagery, the track measures approximately 550 m long and 75 m at its widest point. The track passed through an area of complex terrain with an elevation increase of approximately 54 m (see Fig. 5b). In addition, the resolution of the DSM is so high that even small surface features (such as a small 5-m-deep gully) can be easily identified and used for microscale analysis. In the DSM, there is a small artifact over the water related to the specular reflection related to azimuth angle affecting SfM, but this artifact lies outside the scope of analysis.

VDVI imagery highlights the range of damage relative to topography as well as vegetative health over the survey site (see Fig. 5c). Overall VDVI values in the image are relatively low based on a mean VDVI value of 0.16. There are some higher values (close to 0.40) toward the bottom of the image, indicating healthier vegetation. Within the area of enhanced scour, VDVI values are close to zero, similar to those of bare soil or water (shown in black in Figs. 5c–d), suggesting stressed or damaged vegetation. Areas of enhanced scour can also be seen along the trace (centerline of damage path) in areas of local elevation maxima (see Figs. 5b–d; areas marked "Enhanced Scour"), especially on the upslope side assuming a largely radial near-ground inflow.

Another major change seen in the VDVI image (near the middle of Fig. 5c) is the cessation of a single enhanced scour mark, and beginning of more numerous, diffuse and faint curved markings. In this area, the path traverses between two local elevation maxima. Figure 5d shows that the damage path appears to follow the area of maximum elevation change as the tornado trace crosses the 2-m contours through the steepest elevation gradient. An analysis of the storm-chaser videos available online does not show a dramatic change in tornado

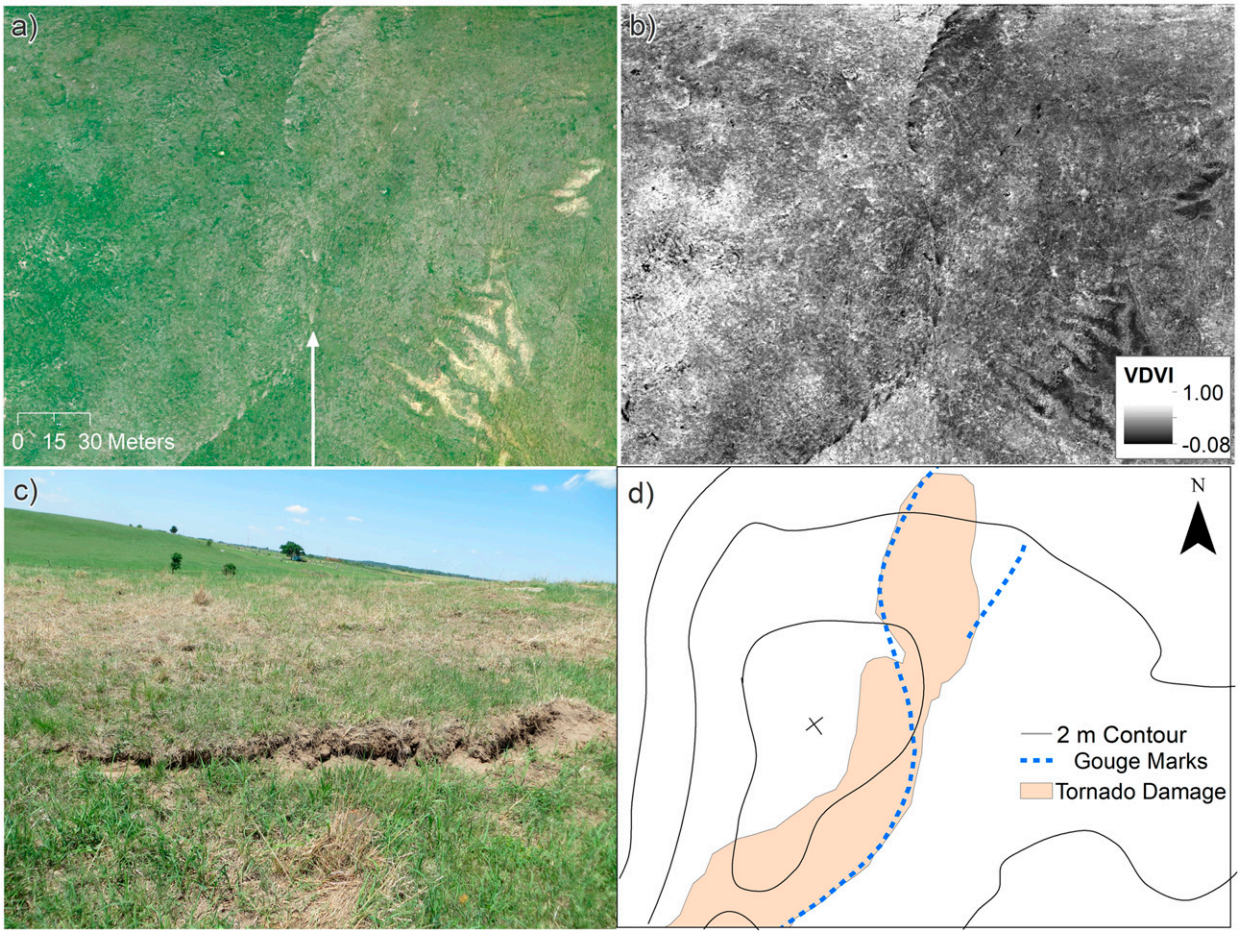

FIG. 8. Path deviation captured in (a) true-color composite image and (b) VDVI image of the 1 May 2018 Tescott tornado survey site at the top of the hill. In (a) and (b), gouge marks (individual pitted effect) in shortgrass prairies have a dashed appearance. The white arrow in (a) points to (c) an individual gouge mark approximately 6–10 cm deep in the ground survey photograph. (d) The 2-m elevation contours (black lines) overlaid onto the tornado-damaged area (orange filled polygon) and gouge marks (blue dashed lines). The black cross in (d) denotes the area of maximum elevation (~430 m).

morphology during this transition. Rather, the tornado remains associated with a large area of ragged condensation with an increase in the visual impression of subvortices at the tornado periphery. Although examination of VDVI data alone cannot be used to fully document tornado kinematics, it certainly appears that prior to the transition there was likely a single-cell (endwall jet) structure near the middle of the larger tornado debris/condensation cloud. A subsidiary vortex would have had a more off-center, trochoidal path, whereas the observed scour marks prior to the transition appear in a consolidated swath with a much smaller radius (<50 vs >1000 m) than the larger-scale damage swath. Nevertheless, a significantly damaging kinematic feature does persist through the transition, and appears to deviate between the terrain maxima before resuming a path consistent with the larger damage path. This behavior does not seem to be consistent with any previously published conceptual models of tornado damage, but certainly highlights the great utility of VDVI imagery in revealing these kinematic features.

When examining the track in finer detail, there is evidence of microtopographic influences within the signature (see Figs. 6–8). Figures 6a–b displays a visible break in the track corresponding to tornadic winds interacting with a gully. Inside the gully, VDVI values are higher (~0.23) (Fig. 6b), suggesting healthy vegetation; outside the gully, VDVI values drop to zero, indicating damaged vegetation. Additionally, surface erosion inside the gully is limited as evidenced by increased surface roughness/texture (Fig. 6c). Outside the gully, there is also visible surface smoothing within the highlighted track (white dashed lines), showing that vegetation has been completely removed (Figs. 6a,c). Elevation changes as measured by slope increase by 20% from the gulley's local minimum elevation (see Fig. 6d) with uniform vegetation cover and no standing water inside the gully (see Fig. 7). Looking at the top of the hill, the path of enhanced scour deviates to the left and cyclic gouge marks commence, suggesting a possible change in wind dynamics and corner flow swirl ratio (see Fig. 8). Interestingly, the track appears to curve around the contour of

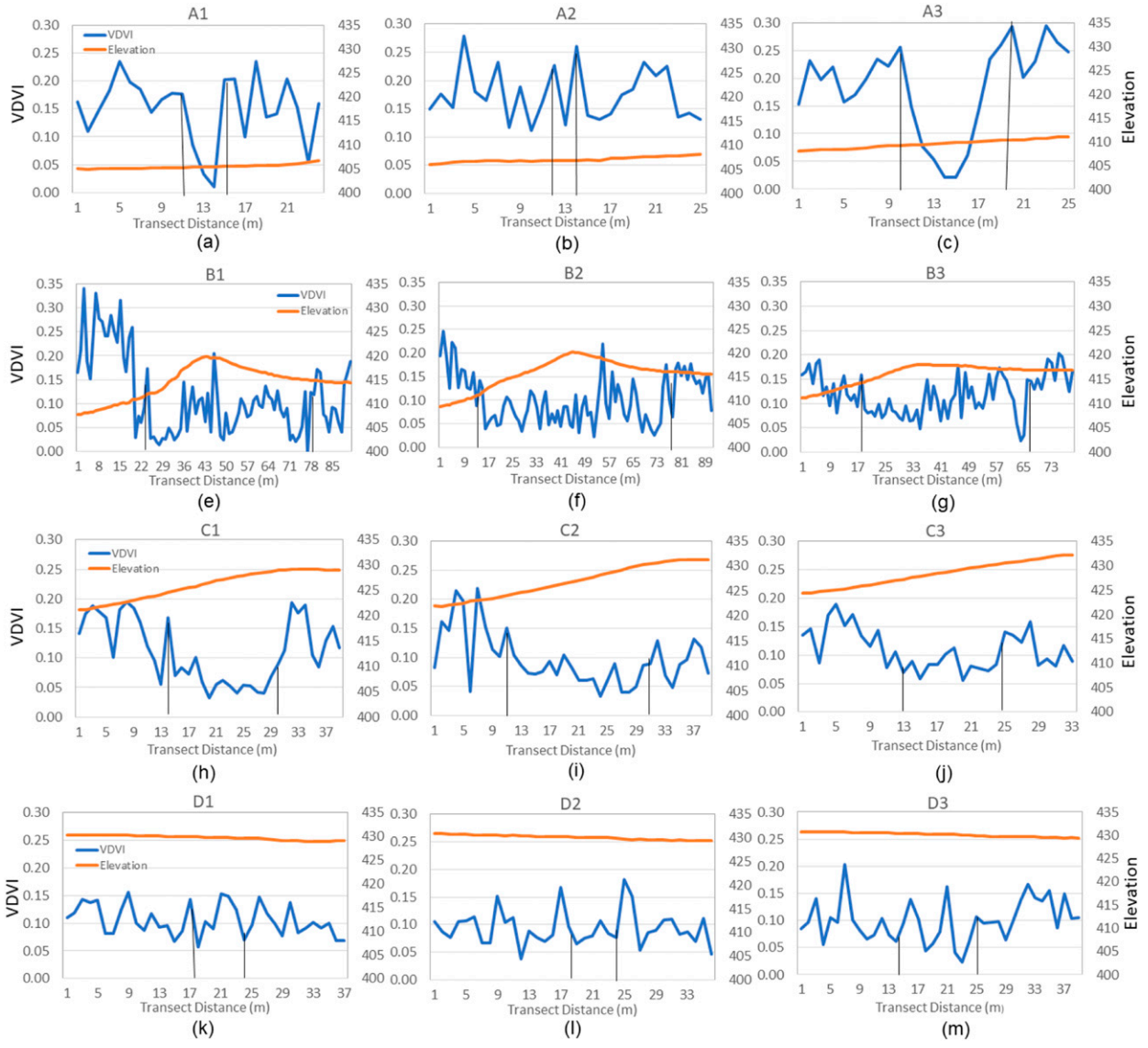

FIG. 9. Mean VDVI and elevation values of the 1 May 2018 Tescott tornado survey site shown in blue and orange, respectively, at selected transects nearly perpendicular to the center of the tornado damage path, as shown in Fig. 4. Mean values are based on a sampling buffer of 0.1-m radius around sampling points at 1-m intervals (see Figs. 2 and 3) along these transects. Solid black vertical lines delineate areas of enhanced scour within the boundary of the tornado-damaged area shown in red in Fig. 2.

local elevation maxima (orange circular line on 8b), suggesting there may have been topographical influence (see Fig. 8b).

b. Transect analysis

Transect analysis (Figs. 4, 9) shows changes in damage severity and path width relative to elevation, as measured by VDVI values. In the case of a small 5-m-deep gully, transects A1–A3 are oriented parallel to the gully where transect A1 is downslope of the gully, transect A2 is inside in the gully, and transect A3 is upslope of the gully. Figure 4 (box A in elevation profile) shows an approximate gain of 5 m in vertical elevation along the centerline of the damage path (area of enhanced scour) with a slight dip in vertical elevation corresponding to the gully. Transects A1 and A3 display VDVI values close to zero within the area of enhanced scour (center of the track) bounded by black vertical lines, whereas transect A2 shows VDVI values of 0.1–0.25 in the center of the track (see Fig. 9). This finding illustrates how tornadic winds can produce varying degrees of damage even relative to microscale changes in elevation.

Transects B1–D3 (Figs. 4, 9) also highlight how landscape and microscale elevation relationships can influence a tornado track. The tornado path widens by approximately 50 m from transects A1–A3 to B1–B3 as the tornado interacts with terrain near a local elevation maximum at 420 m above mean sea level (MSL) (see Figs. 4, 9). In this area, VDVI values decrease to an

TABLE 1. Correlation analysis between relevant pairs of variables.

Variable pair	2.5-percentile correlation limit	97.5-percentile correlation limit	Bootstrap mean correlation	Significant correlation
Elevation–VDVI gap	− 0.830	− 0.486	− 0.705	Yes
Slope–VDVI gap	0.279	0.699	0.534	Yes
Elevation–path width	− 0.195	0.567	0.234	No
Slope–path width	0.013	0.618	0.342	Yes
Elevation–VDVI aspect ratio	− 0.882	− 0.624	− 0.791	Yes
Slope–VDVI aspect ratio	− 0.100	0.421	0.172	No

average of 0.06 in the areas of enhanced scour (solid lines in Figs. 9a–f). Similar decreases in VDVI values are also observed near the elevation maximum (transects C1–C3) and appear to follow the microscale elevation gradient, where the elevation increases to 430 m, increasing by 10 m along the transect from left to right (see Figs. 4, 9). As elevation levels out (transects D1–D3 in Figs. 4, 9), microtopography appears to play less of an influence in track dynamics. The tornado track becomes less defined and changes from linear to nonlinear in the flat terrain at 430 m (see Figs. 4, 9).

c. *Correlation analysis*

Table 1 shows the results of nonparametric bootstrap correlation analysis against both elevation and slope across all three damage measures. Damage severity, as measured by VDVI gap and VDVI aspect ratio, and elevation are modestly correlated. Here, the existence of a moderate relationship shows that tornado dynamics (and so damage) as measured by VDVI gap and VDVI aspect ratio is indeed affected by terrain. Other statistically nonzero correlations (i.e., slope and VDVI gap; slope and path width) are relatively weak, while there is no clear relationship between path and elevation, nor VDVI aspect ratio and slope.

Figure 10 shows the relationships of damage severity (i.e., VDVI gap and VDVI aspect ratio) with elevation and slope and path width with slope. Only parameters with significant correlations are shown (Table 1). Damage severity, as measured by VDVI gap, shows a weakly positive relationship with

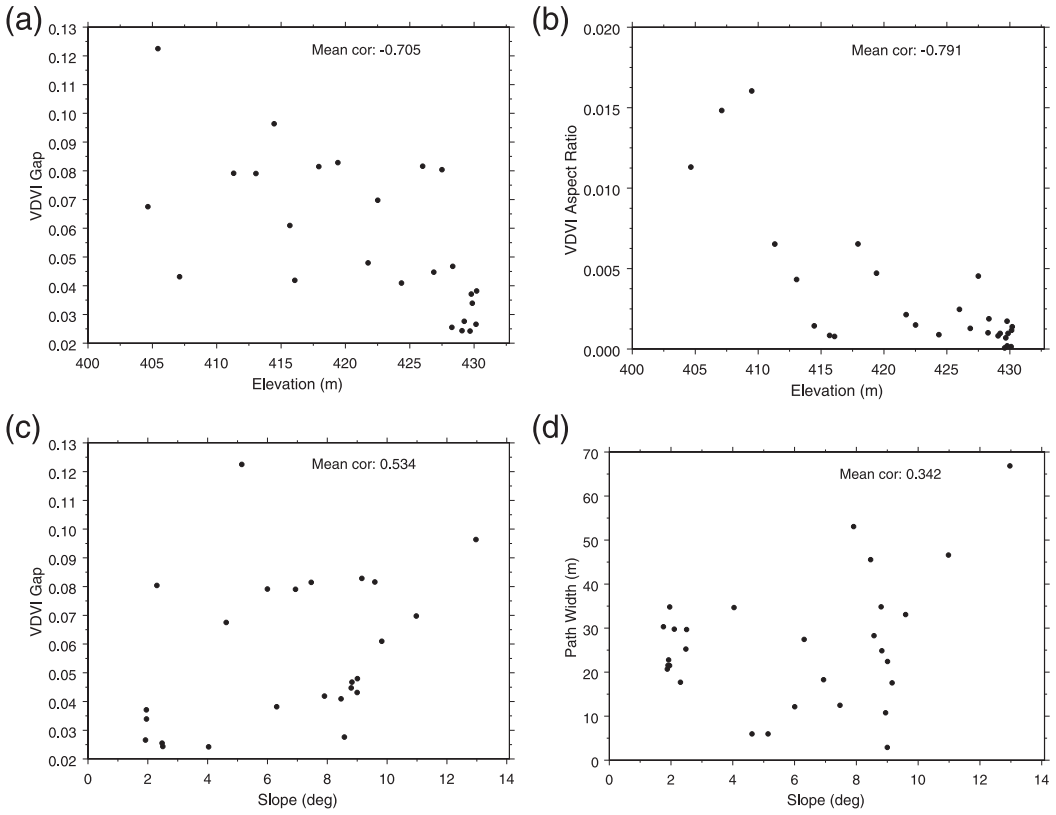

FIG. 10. Scatterplots showing the mean correlation of the bootstrap samples between (a) VDVI gap and elevation, (b) VDVI aspect ratio and elevation, (c) VDVI gap and slope, and (d) path width and slope.

slope (Fig. 10a) and a negative relationship with elevation (Fig. 10b), indicating damage severity decreases in areas of lower slope (flatter terrain) and with increasing elevation. While both relationships are statistically significant at p value < 0.05, there is a much stronger relationship with elevation (see Fig. 10b.) The relationship between VDVI aspect ratio is even stronger (Fig. 10c), yet the relationship between VDVI aspect ratio and slope is indistinguishable from zero (not shown).

5. Discussion

The 1 May 2018 Tescott EF3 tornado survey site (see Fig. 1) provided a unique opportunity to examine the association of microtopographical features with damage path characteristics using UAS technologies and geospatial techniques. These findings show that damage severity, as measured by VDVI gap and VDVI aspect ratio, decreased with increasing elevation, similar to the findings of Forbes (1998), Coleman (2010), Lewellen (2012), Karstens (2012), and Lyza and Knupp (2014). This relationship was statistically significant at $p < 0.05$. When examining VDVI aspect ratio, the relationship between damage severity (VDVI gap), path width, and elevation becomes more evident. VDVI aspect ratio shows a strong negative relationship with increasing elevation (see Fig. 10b). This finding suggests damage gradient is large but localized at lower elevations and near local elevation minima as evidenced by enhanced-scoured regions and narrow path widths. At higher elevations and near local elevation maxima, damage gradient is small and spread out over a larger area as indicated by mildly scoured regions and wider path width. This finding suggests that tornado intensity is high near the beginning of the tornado path as shown by a deep but narrow damage swath into the hillside (see Fig. 4). As the tornado climbs the hillside, tornado intensity decreases with nominal damage and the damage swath widening into the hillside.

The findings of this study show that even microscale landforms and changes in elevation can have a detectable influence on damage severity and path characteristics. For example, the small 5-m-deep gully landform illustrates how tornadic winds can produce varying degrees of damage relative to even small changes in elevation, with minimal to no damage observed inside the gully and areas of denuded vegetation outside the gully. In this case, at least, the historical advice of seeking shelter in a ditch or depression, in the absence of safer shelter, seems to be well founded. In areas of local elevation maxima, path width increased as evidenced by mildly scoured regions (lower VDVI values) despite decreasing damage severity (lower VDVI gap values). The reason for this is unclear and likely complex, but perhaps can be explained by the protrusion of the local terrain more deeply into the intense tornado inflow.

Where elevation plateaued, damage severity decreased considerably with the damage path becoming less defined and changing from linear to more variable in shape. This variable shape could be partially explained by terrain-induced path deviation. As the vortex climbs the hill, the central axis of the tornado remains perpendicular to the terrain, but the lower end of the vortex accelerates and tilts backward causing the path to deviate to the left, similar to the discussion by Lewellen (2012) and Satrio et al. (2020). Additionally, the damage path could have been influenced by landform as it appeared to follow the elevation contour between two local elevation maxima (see Fig. 5d). This finding is similar to Lyza and Knupp (2014) and Cannon et al. (2016), who observed slight deviations in tornado tracks coincident with the edge of plateaus or valley channels. Of course, terrain is only one influence, and perhaps a minor one. For example, this analysis cannot assess the relative impact of the evolution of the parent vortex (e.g., Rasmussen and Straka 2007; Markowski et al. 2012; Marquis et al. 2016) or nearby processes such as internal surges in the rear-flank downdraft (Hirth et al. 2008; Marquis et al. 2008; Lee et al. 2011). However, the nonlinear path noted here is a local, fairly small-scale deviation in an otherwise long and fairly straight damage path, so perhaps the association with local terrain is important. These findings highlight how topography possibly plays a significant role in understanding the intensity and variability of the tornado damage path.

This study also presents an interesting case study into the complicated kinematics of tornadoes as the tornado path becomes nonlinear. In the linear segment, we hypothesize that intense swirling flow was likely located at or near the axis of the tornado and moving with the mesocyclone as the tornado climbed up the hill. During the enhanced scour, the tornado was probably a single-celled vortex on the ground with very high wind speeds and an intense upward jet. This could explain the linear segment of denuded vegetation (deep scour) and high VDVI gap values near the beginning of the track as nontrochoidal track segments have been noted to occur when the tornado is located at or near the center of the mesocyclone (e.g., Wakimoto et al. 2003). As the tornado climbed up the hill, vortex intensity decreased. This could partially explain the decrease in damage severity (lower VDVI gap and VDVI aspect ratio values). It can be hypothesized that, near the top of the hill, the vortex likely transitioned into a two-celled vortex with the kinematic feature of intense flow moving out in front of the axis and the path deviated.

One of the remarkable and seemingly unexplainable phenomena revealed in this analysis is the cyclic-like gouge marks that began at what appears to be the terminus of the single-cell enhanced scour mark (Fig. 8). These gouges were observed to be about 6–10 cm deep during a ground survey of the track. One hypothesis is that a large piece of bouncing debris produced these marks, but that hypothesis becomes dubious as the path resumes its northeastward orientation and the marks continue. One would expect the bouncing object to orbit back toward the rear and right side of the path, and not linger more toward the left side. The marks are too close together to be considered to be a trochoidal effect with a tornado moving this quickly, unless they were produced by multiple flow enhancements orbiting the tornado at fairly constant spacing. Further, one would expect subvortices producing trochoidal enhancements would be occurring at a much larger radius (note the overall damage path is much wider than the phenomena producing these marks, likely near the tornado axis). Perhaps future studies using this sort of instrumentation will clarify the origins of marks such as

these and illuminate whether they indeed represent a local extreme wind phenomenon associated with the tornado.

This study also demonstrates the benefits of utilizing UAS technologies and geospatial techniques in site surveys (assessments of tornado damage) (e.g., Skow and Cogil 2017; Wagner et al. 2019). UAS high-resolution imagery provides centimeter-scale damage information that can be used to identify small-scale features such as local elevation maximum and minimum (i.e., the gully shown) as well as debris marks. The 3D modeling capabilities also provide high-resolution (centimeter scale) elevation information, which can be used to examine topographic influences on damage path characteristics as well as other land cover interactions at the microscale. By using UAS-based information in conjunction with geospatial techniques, estimates of damage path characteristics can be refined through additional damage information (e.g., surface roughness and VDVI imagery) and more precise measurements (track width and length) as shown in this study.

Geospatial techniques (i.e., VDVI imagery and transect analysis) proved especially useful in assessing damage severity within the track and relative to elevation as demonstrated by this study. In particular, VDVI imagery better captured the range of damage by assessing vegetative health over the survey site. Overall, VDVI values were generally low (a mean of 0.2) due to the land cover type consisting of predominantly short-grass prairies. In areas affected by tornadic winds, VDVI values dropped to a mean of 0.10, indicating areas of stressed vegetation. In areas of enhanced scour, VDVI values dropped close to 0, similar to those of bare soil and water, pointing to areas of denuded vegetation. These findings indicate the ability to detect vegetation damage based on the spectral response of vegetation in the red and green bands, even when near-infrared information is unavailable. Such detailed information could enable the development of more damage indicators for vegetation that are more reflective of tornadic intensity in rural areas (Snyder and Bluestein 2014; Wagner et al. 2019). In addition, the two new metrics, VDVI gap and VDVI aspect ratio, introduced here, can provide insight into damage variability within the track and relative to elevation. In other cases, these metrics can be used in satellite imagery analysis to investigate the influence of tornadic winds on land cover.

6. Conclusions

Fundamentally, a set of primary conclusions can be identified as follows: 1) Microscale landforms and changes in elevation can have a detectable influence on damage severity and path width as seen in the cases of the gulley and top of the hill. 2) Damage severity decreased with increasing elevation on the windward side and in areas of steeper slope. 3) VDVI aspect ratio shows a strong negative relationship with increasing elevation, indicating (i) high damage severity and narrow path widths at lower elevations and near local elevation minimum and (ii) low damage severity and wider path widths at higher elevations and near local elevation maxima. 4) UAS technologies can provide detailed 2D and 3D information for local site surveys and microscale analysis. 5) Geospatial techniques (e.g., VDVI imagery, transect analysis) proved especially useful in assessing damage severity and variability within the track and relative to elevation.

Future work should examine additional case studies to validate the findings of this individual study, especially given the site-specific characteristics of tornado events. Additional studies are also needed to investigate high wind interactions with other landforms and land cover features (e.g., land use and vegetation type). Specifically, comprehensive assessments involving multiple observation datasets (e.g., in situ measurements, radar data, and damage information) could improve our understanding of wind dynamics and land cover influences by relating changes in kinematic structures to observed damage. Such assessments would improve our understanding of how site-specific characteristics (e.g., land cover and terrain) can influence tornadoes and damage path characteristics and would present another layer of enhanced methodology toward holistic tornado site investigations. This detailed information would also enable a better estimation of near surface wind speeds with tornadic winds, which could lead to better damage mitigation strategies for a more resilient society.

Acknowledgments. Current Funding for authors Wagner and Rasmussen is provided through the NOAA/Office of Oceanic and Atmospheric Research under NOAA–University of Oklahoma Cooperative Agreement NA11OAR4320072, U.S. Department of Commerce. The authors thank Dean Martin, the property owner at Tescott, for access and permission for UAS flights and David Baxter for footage of the 1 May 2018 Tescott tornado at the survey site.

Data availability statement. All of the data collected and analyzed for this study and further information about data processing are available upon request from the first author (melissa.a.wagner@noaa.gov).

REFERENCES

Agisoft, 2019: Agisoft Metashape user manual: Professional edition version 1.5. Agisoft LLC Doc., 145 pp., https://www.agisoft.com/pdf/metashape-pro_1_5_en.pdf.

Ahmed, N. S., 2016: Field observations and computer modeling of tornado-terrain interaction and its effects on tornado damage and path. Ph.D. dissertation, The University of Arkansas, 247 pp., http://scholarworks.uark.edu/etd/1463.

Bosart, L. F., A. Seimon, K. D. LaPenta, and M. J. Dickinson, 2006: Supercell tornadogenesis over complex terrain: The Great Barrington, Massachusetts, tornado on 29 May 1995. *Wea. Forecasting*, **21**, 897–922, https://doi.org/10.1175/WAF957.1.

Cannon, J. B., J. Hepinstall-Cymerman, C. M. Godfrey, and C. J. Peterson, 2016: Landscape-scale characteristics of forest tornado damage in mountainous terrain. *Landscape Ecol.*, **31**, 2097–2114, https://doi.org/10.1007/s10980-016-0384-8.

Carlson, T. N., and D. A. Ripley, 1997: On the relation between NDVI, fractional vegetation cover, and leaf area index. *Remote Sens. Environ.*, **62**, 241–252, https://doi.org/10.1016/S0034-4257(97)00104-1.

Carrivick, J. L., M. W. Smith, and D. J. Quincey, 2016: *Structure from Motion in the Geosciences*. John Wiley and Sons, 197 pp.

Chen, Q. J., Y. R. He, T. T. He, and W. J. Fu, 2020: The typhoon disaster analysis emergency response system based on UAV

remote sensing technology. *Int. Arch. Photogramm. Remote Sens. Spat. Info. Sci.*, **XLII-3/W10**, 959–965, https://doi.org/10.5194/isprs-archives-XLII-3-W10-959-2020.

Coleman, T. A., 2010: The effects of topography and friction on mesocyclones and tornadoes. *25th Conf. on Severe Local Storms*, Denver, CO, Amer. Meteor. Soc, P8.12, https://ams.confex.com/ams/25SLS/techprogram/paper_176240.htm.

DiCiccio, T. J., and J. P. Romano, 1990: Nonparametric confidence limits by resampling methods and least favorable families. *Int. Stat. Rev.*, **58**, 59–76, https://doi.org/10.2307/1403474.

Doe, R., and M. Wagner, 2019: Tornado pathway dynamics using UAS: The influence of topography on tornadoes. *35th Conf. on Environmental Information Processing Technologies*, Phoenix, AZ, Amer. Meteor. Soc., J1.3, https://ams.confex.com/ams/2019Annual/meetingapp.cgi/Paper/353002.

Du, M., and N. Noguchi, 2017: Monitoring of wheat growth status and mapping of wheat yield's within-field spatial variations using color images acquired from UAV-camera system. *Remote Sens.*, **9**, 289, https://doi.org/10.3390/rs9030289.

Efron, B., 1981: Nonparametric standard errors and confidence intervals. *Can. J. Stat.*, **9**, 139–158, https://doi.org/10.2307/3314608.

——, and R. J. Tibshirani, 1994: *An Introduction to the Bootstrap*. Chapman and Hall, 436 pp.

Ezequiel, C. A. F., and Coauthors, 2014: UAV aerial imaging applications for post-disaster assessment, environmental management and infrastructure development. *Int. Conf. on Unmanned Aircraft Systems*, Orlando, FL, IEEE, 274–283.

Forbes, G. S., 1998: Topographic influences on tornadoes in Pennsylvania. Preprints, *19th Conf. on Severe Local Storms*, Minneapolis, MN, Amer. Meteor. Soc., 269–272.

Heredia, G., F. Caballero, I. Maza, L. Merino, A. Viguria, and A. Ollero, 2009: Multi-unmanned aerial vehicle (UAV) cooperative fault detection employing differential global positioning (DGPS), inertial and vision sensors. *Sensors*, **9**, 7566–7579.

Hesterberg, T. C., 1999: Bootstrap tilting confidence intervals and hypothesis tests. *Comput. Sci. Stat.*, **31**, 389–393.

Hirth, B. D., J. L. Schroeder, and C. C. Weiss, 2008: Surface analysis of the rear-flank downdraft outflow in two tornadic supercells. *Mon. Wea. Rev.*, **136**, 2344–2363, https://doi.org/10.1175/2007MWR2285.1.

Houser, J. B., N. McGinnis, K. M. Butler, H. B. Bluestein, J. C. Snyder, and M. M. French, 2020: Statistical and empirical relationships between tornado intensity and both topography and land cover using rapid-scan radar observations and a GIS. *Mon. Wea. Rev.*, **148**, 4313–4338, https://doi.org/10.1175/MWR-D-19-0407.1.

Huang, J., 2018: Assessment of potential changes in soil erosion using remote sensing and GIS: A case study of Dacaozi Watershed, China. *Environ. Monit. Assess.*, **190**, 736, https://doi.org/10.1007/s10661-018-7120-6.

Johnson, K., E. Nissen, S. Saripalli, J. R. Arrowsmith, P. McGarey, K. Scharer, and K. Blisniuk, 2014: Rapid mapping of ultrafine fault zone topography with structure from motion. *Geosphere*, **10**, 969–986, https://doi.org/10.1130/GES01017.1.

Karstens, C. D., 2012: Observations and laboratory simulations of tornadoes in complex topographical regions. Ph.D. dissertation, The Iowa State University, 155 pp., https://lib.dr.iastate.edu/etd/12778.

Kingfield, D. M., and K. M. de Beurs, 2017: Landsat identification of tornado damage by land cover and an evaluation of damage recovery in forests. *J. Appl. Meteor. Climatol.*, **56**, 965–987, https://doi.org/10.1175/JAMC-D-16-0228.1.

Lee, B. D., C. A. Finley, and T. M. Samaras, 2011: Surface analysis near and within the Tipton, Kansas, tornado on 29 May 2008. *Mon. Wea. Rev.*, **139**, 370–386, https://doi.org/10.1175/2010MWR3454.1.

Lewellen, D. C., 2012: Effects of topography on tornado dynamics: A simulation study. *26th Conf. on Severe Local Storms*, Nashville, TN, Amer. Meteor. Soc. 4B.1, https://ams.confex.com/ams/26SLS/webprogram/Paper211460.html.

——, and W. S. Lewellen, 2007: Near-surface intensification of tornado vortices. *J. Atmos. Sci.*, **64**, 2176–2194, https://doi.org/10.1175/JAS3965.1.

Lyza, A. W., and K. R. Knupp, 2014. An observational analysis of potential terrain influences on tornado behavior. *27th Conf. on Severe Local Storms*, Madison, WI, Amer. Meteor. Soc., 11A.1A, https://ams.confex.com/ams/27SLS/webprogram/Paper255844.html.

Markowski, P., and Coauthors, 2012: The pretornadic phase of the Goshen County, Wyoming, supercell of 5 June 2009 intercepted by VORTEX2. Part II: Intensification of low-level rotation. *Mon. Wea. Rev.*, **140**, 2916–2938, https://doi.org/10.1175/MWR-D-11-00337.1.

Marquis, J., Y. Richardson, J. Wurman, and P. Markowski, 2008: Single- and dual-Doppler analysis of a tornadic vortex and surrounding storm-scale flow in the Crowell, Texas, supercell of 30 April 2000. *Mon. Wea. Rev.*, **136**, 5017–5043, https://doi.org/10.1175/2008MWR2442.1.

——, ——, P. Markowski, J. Wurman, K. Kosiba, and P. Robinson, 2016: An investigation of the Goshen County, Wyoming, tornadic supercell of 5 June 2009 using EnKF assimilation of mobile mesonet and radar observations collected during VORTEX2. Part II: Mesocyclone-scale processes affecting tornado formation, maintenance, and decay. *Mon. Wea. Rev.*, **144**, 3441–3463, https://doi.org/10.1175/MWR-D-15-0411.1.

McHarg, I. L., 1969: *Design with Nature*. American Museum of Natural History, 197 pp.

NOAA/National Centers for Environmental Information, 2020: Storm events database (1 May 2018, Tescott Kansas). NOAA, accessed 10 March 2020, https://www.ncdc.noaa.gov/stormevents/eventdetails.jsp?id=743852.

Passe-Smith, M. S., 2006: Exploring local ''tornado alleys'' for predictive environmental parameters. *Proc. 2006 ESRI Int. User Conf.*, ESRI, 28 pp., https://proceedings.esri.com/library/userconf/proc06/papers/papers/pap_1339.pdf.

——, 2008: Effect of topography on weak and moderate tornadoes. *Proc. 2008 ESRI Int. Users Conf.*, ESRI, 21 pp., https://proceedings.esri.com/library/userconf/proc08/papers/papers/pap_1396.pdf.

Rasmussen, E. N., and J. M. Straka, 2007: Evolution of low-level angular momentum in the 2 June 1995 Dimmitt, Texas, tornado cyclone. *J. Atmos. Sci.*, **64**, 1365–1378, https://doi.org/10.1175/JAS3829.1.

Satrio, M. A., D. J. Bodine, A. E. Reinhart, T. Maruyama, and F. T. Lombardo, 2020: Understanding how complex terrain impacts tornado dynamics using a suite of high-resolution numerical simulations. *J. Atmos. Sci.*, **77**, 3277–3300, https://doi.org/10.1175/JAS-D-19-0321.1.

Skow, K. D., and C. Cogil, 2017: High-Resolution aerial survey and radar analysis of quasi-linear convective system surface vortex damage paths from 31 August 2014. *Wea. Forecasting*, **32**, 441–467, https://doi.org/10.1175/WAF-D-16-0136.1.

Snyder, J. C., and H. B. Bluestein, 2014: Some considerations for the use of high-resolution mobile radar data in tornado intensity determination. *Wea. Forecasting*, **29**, 799–827, https://doi.org/10.1175/WAF-D-14-00026.1.

Tmušić, G., and Coauthors, 2020: Current practices in UAS-based environmental monitoring. *Remote Sens.*, **12**, 1001, https://doi.org/10.3390/rs12061001.

Tyrrell, T., 2016: Site investigations of tornado events. *Extreme Weather: Forty Years of the Tornado and Storm Research Organisation*, R. K. Doe, Ed., John Wiley and Sons, 91–104.

Wakimoto, R. M., H. V. Murphey, D. C. Dowell, and H. B. Bluestein, 2003: The Kellerville tornado during VORTEX: Damage survey and Doppler radar analyses. *Mon. Wea. Rev.*, **131**, 2197–2221, https://doi.org/10.1175/1520-0493(2003)131<2197:TKTDVD>2.0.CO;2.

Wagner, M., and R. K. Doe, 2017: Using Unmanned Aerial Vehicles (UAVs) to model tornado impacts. *2017 Fall Meeting*, San Francisco, CA, Amer. Geophys. Union, Abstract NH31A-0198.

——, ——, A. Johnson, Z. Chen, J. Das, and R. S. Cerveny, 2019: Unpiloted aerial systems (UASs) application for tornado damage surveys: Benefits and procedures. *Bull. Amer. Meteor. Soc.*, **100**, 2405–2409, https://doi.org/10.1175/BAMS-D-19-0124.1.

Wang, X., M. Wang, S. Wang, and Y. Wu, 2015: Extraction of vegetation information from visible unmanned aerial vehicle images. *Nongye Gongcheng Xuebao*, **31**, 152–159, https://doi.org/10.3969/j.issn.1002-6819.2015.05.022.

Westoby, M. J., J. Brasington, N. F. Glasser, M. J. Hambrey, and J. M. Reynolds, 2012: 'Structure-from-Motion' photogrammetry: A low-cost, effective tool for geoscience applications. *Geomorphology*, **179**, 300–314.

Womble, J. A., R. L. Wood, and M. E. Mohammadi, 2018: Multiscale remote sensing of tornado effects. *Front. Built Environ.*, **4**, 66, https://doi.org/10.3389/fbuil.2018.00066.

Xue, J., and B. Su, 2017: Significant remote sensing vegetation indices: A review of developments and applications. *J. Sens.*, **2017**, 1–17, https://doi.org/10.1155/2017/1353691.